Supplement of Atmos. Chem. Phys., 26, 16719–16739, 2026
https://doi.org/10.5194/acp-26-16719-2026-supplement
© Author(s) 2026. CC BY 4.0 License.



Atmospheric Chemistry and Physics
Open Access
EGU

Supplement of

Marine organic aerosols reflect ecosystem variability from phytoplankton functional types to micronekton

Emmanuel Chevassus et al.

Correspondence to: Jurgita Ovadnevaite (jurgita.ovadnevaite@universityofgalway.ie)

The copyright of individual parts of the supplement might differ from the article licence.

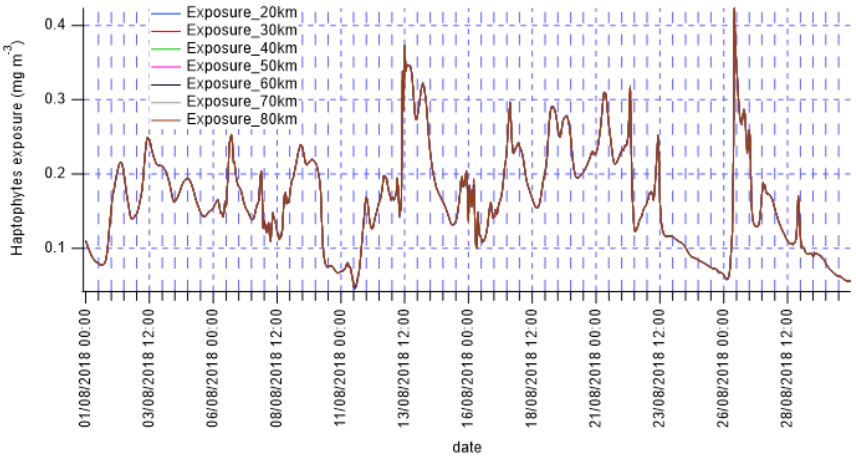

Figure S1. PFTs air-mass exposure was calculated by integrating surface concentrations along back trajectories using circular sampling radii of 20, 40, 60, and 80 km around each HYSPLIT trajectory point to check for spatial sampling scale sensitivity.

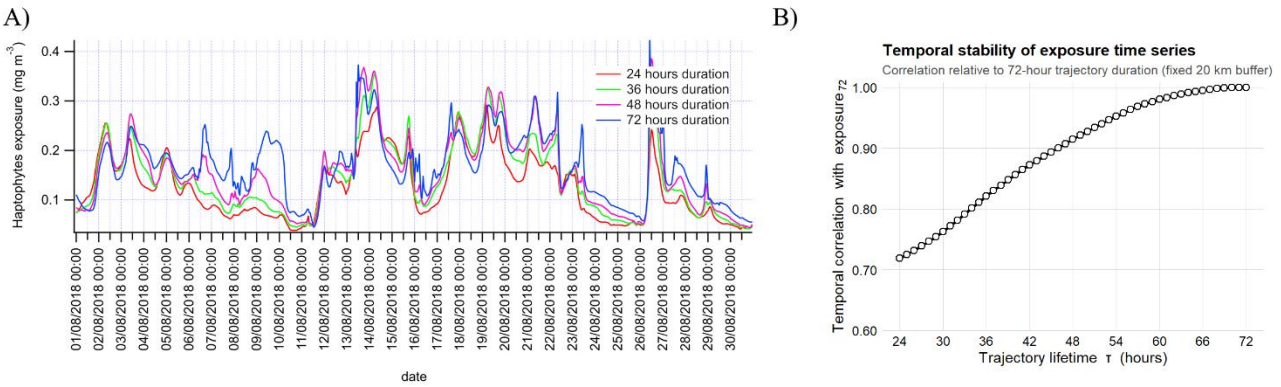

Figure S2. Sensitivity of haptophytes exposure to trajectory lifetime. A) Time series using back-trajectories durations of 24 h (red), 36 h (magenta), 48 h (green) and 72 h (blue). B) Temporal correlation (Pearson´s R) between exposure time series computed with each duration τ and the 72-h reference case.

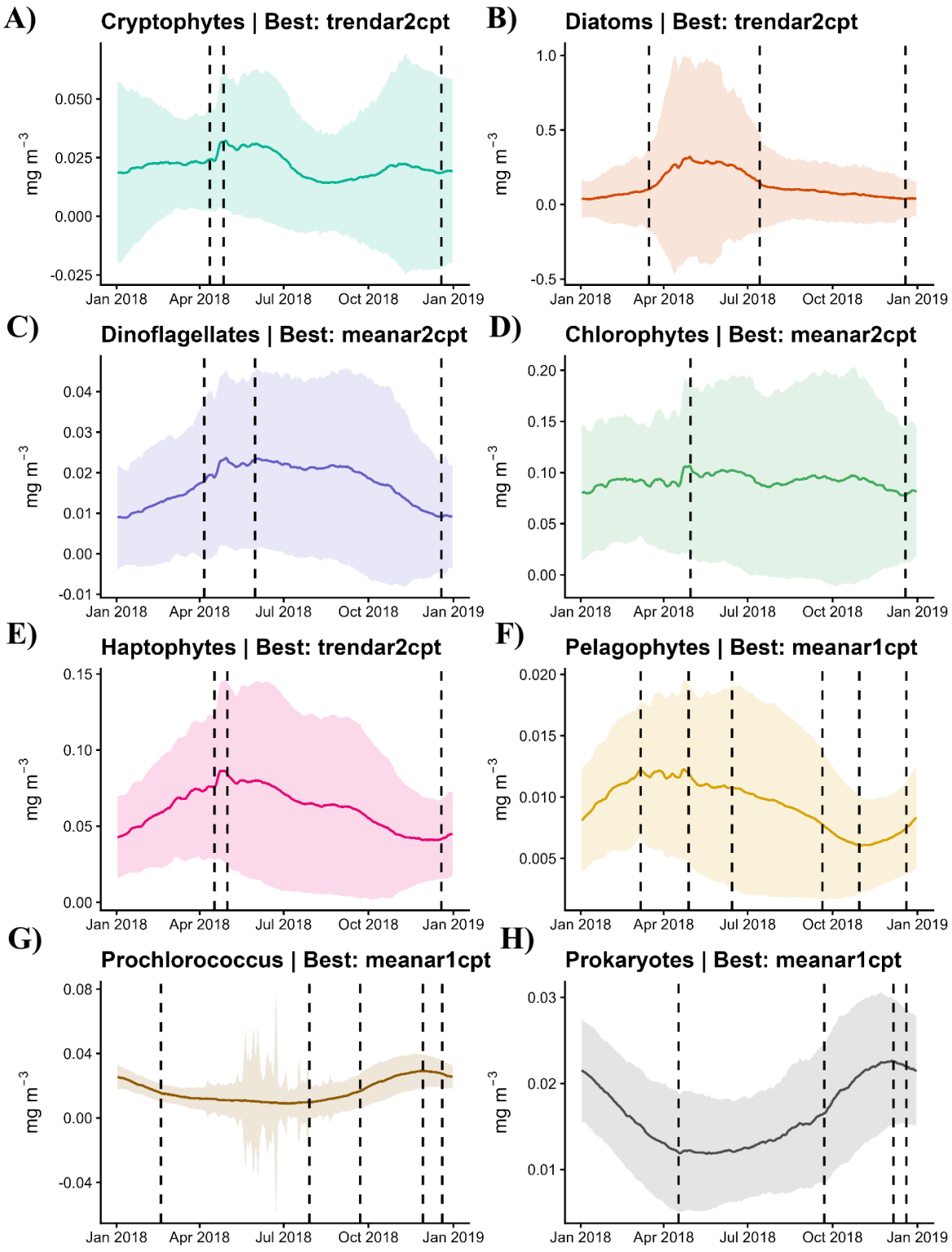

Figure S3. Daily Temporal dynamics of phytoplankton functional types in the North Atlantic extracted from the AIGD-PFT model (Zhang *et al*. 2024). Yearly time series of chl-*a* biomass (mg m⁻³) for major phytoplankton functional types averaged over the region bounded by 20°-66°N and 72°W-0° longitude, similarly to Mansour *et al*. (2024). Panels show: (A) Cryptophytes, (B) Diatoms, (C) Dinoflagellates, (D) Chlorophytes, (E) Haptophytes, (F) Pelagophytes, (G) *Prochlorococcus*, (H) Other Prokaryotes. Shaded areas represent variability (standard deviation) around the mean (negative values are not meaningful), vertical dashed lines denote detected changepoints.

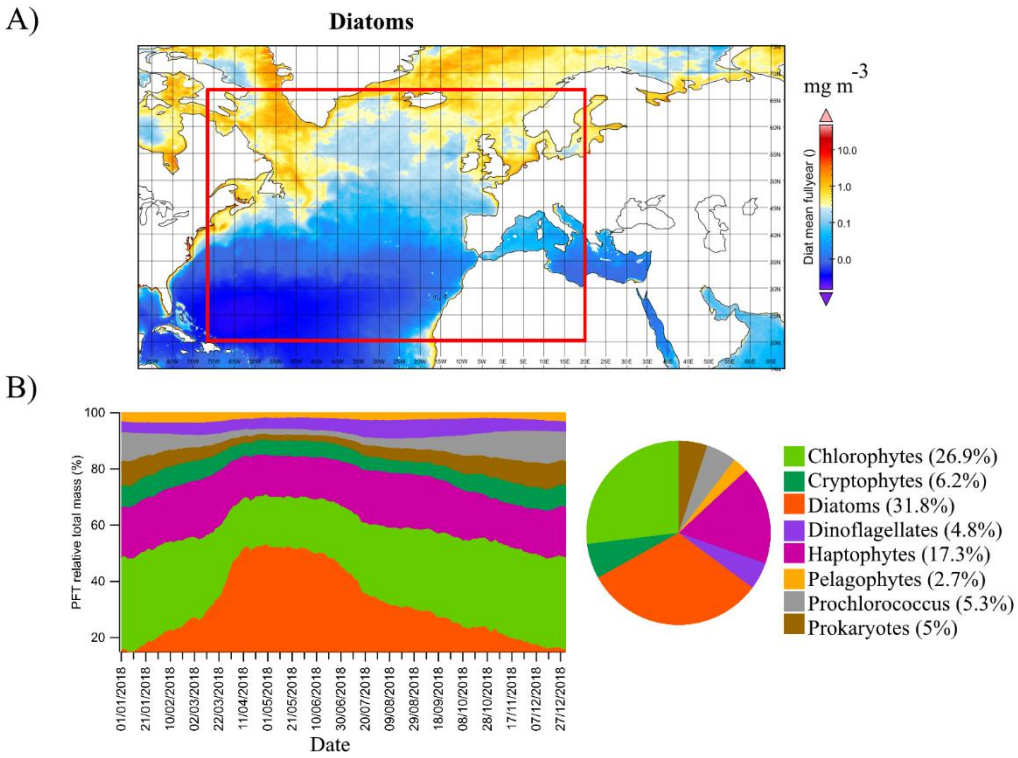

Figure S4. (A) AIGD-PFT Annual mean diatom mass concentrations averaged over the region 20°-66° N, 72° W-0° E. (B) Relative contributions of individual phytoplankton functional types to total chlorophyll-a biomass (sum of the 8 PFTs) within the same region.

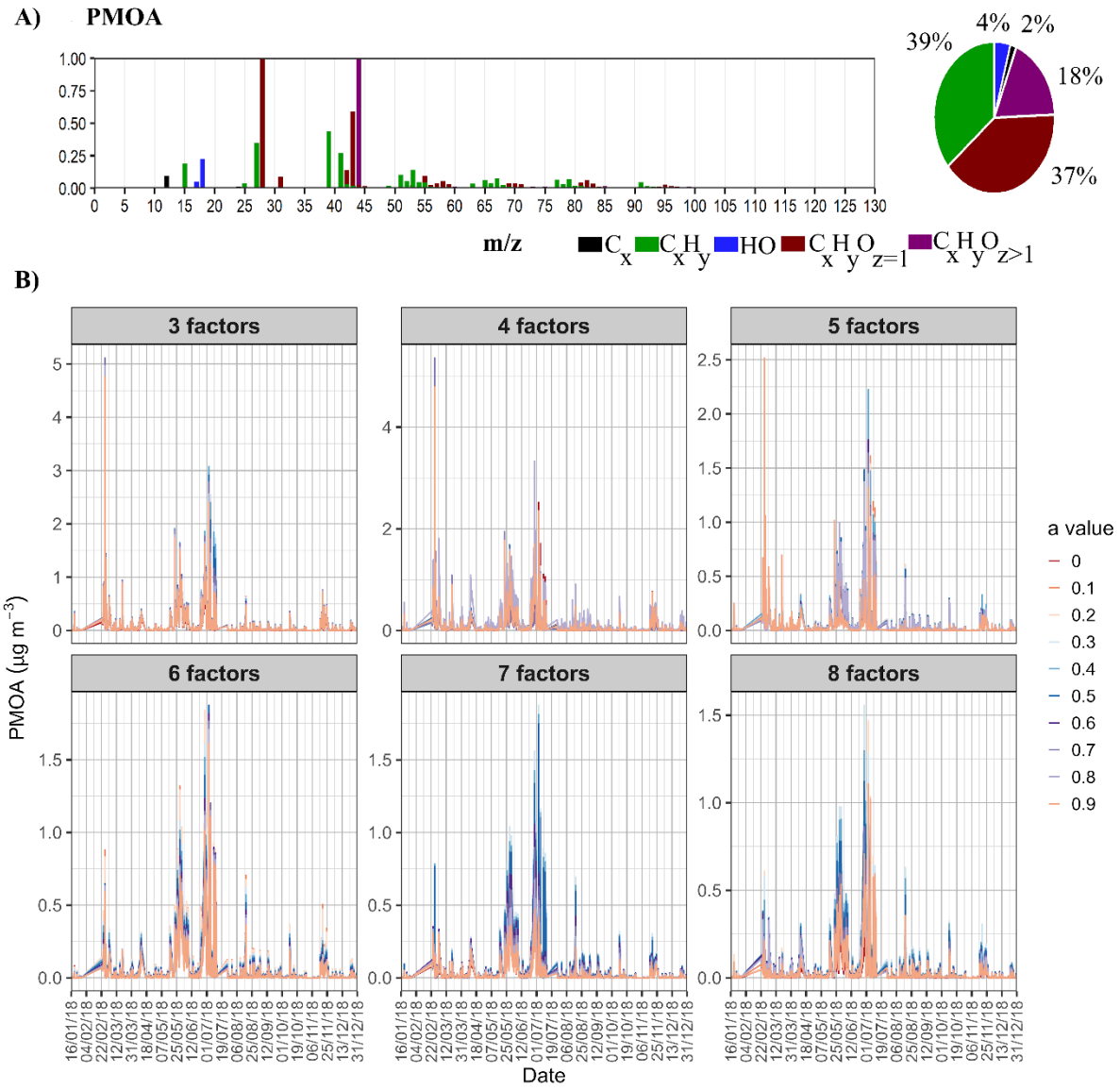

Figure S5. (A) Mass spectra constrained using the Ovadnevaite *et al.* (2011) reference profile. (B) Corresponding PMOA (µg m⁻³) time series reconstructed from PMF solutions ranging from 3 to 8 factors, with a-value variation (0–0.9)

40

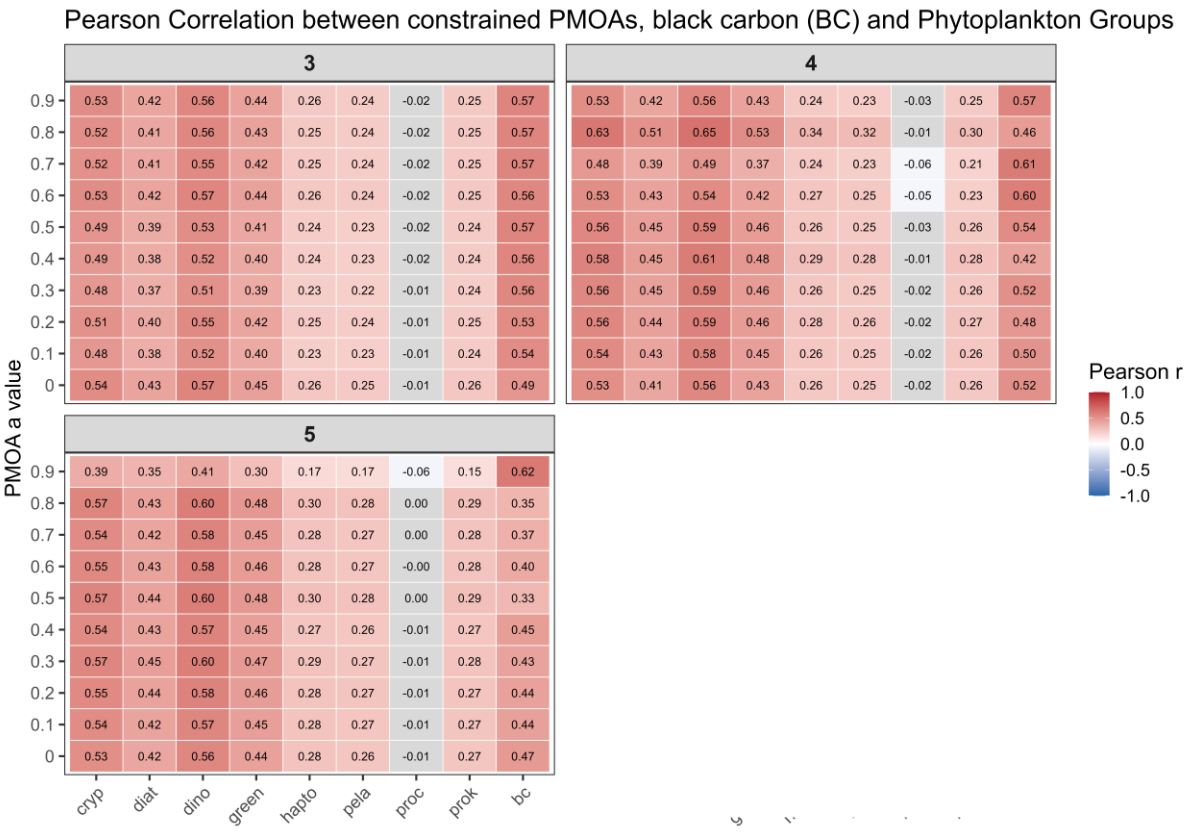

Figure S6. Pearson correlations between constrained PMOA time series and phytoplankton functional types (PFTs) and black carbon (BC) for PMF solutions within 3 to 5 factors. Rows show the a-value used to constrain the PMOA reference spectrum and columns the external variables. Values indicate Pearson correlation coefficients (R). Colours denote significant correlations ($p < 0.05$), while non-significant correlations are shown in grey.

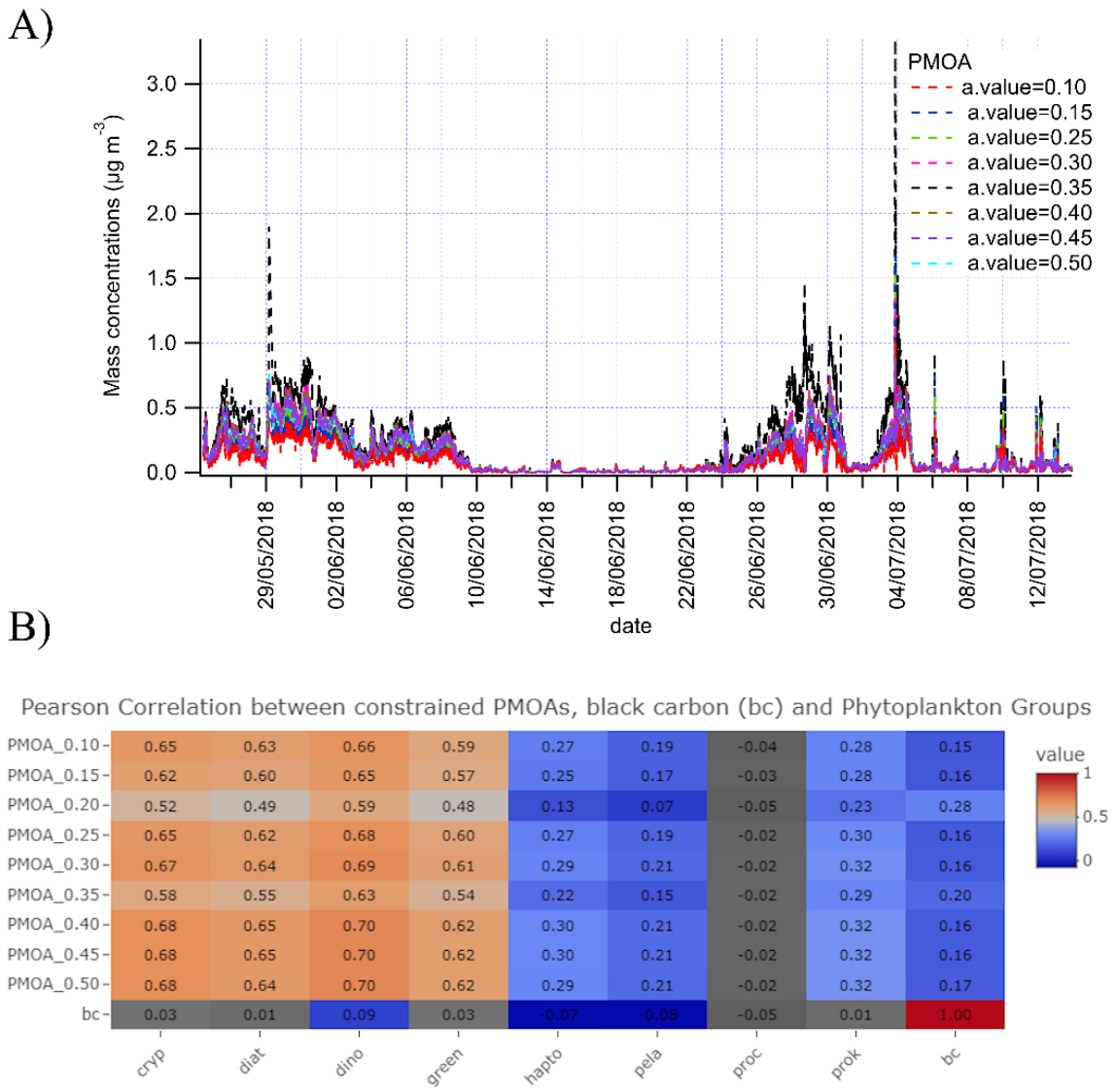

Figure S7. A) Primary marine organic aerosol (PMOA) sensitivity to a-values constraining B) Retained PMOA time series (a-value of 0.40) along with Phytoplankton functional types exposure with retained phytoplankton functional types (cryptophytes, dinoflagellates, diatoms and chlorophytes). B) Pearson´s correlations between primary marine organic aerosol (PMOA) constraining sensitivity analysis time series (a-values), black carbon (bc) and phytoplankton functional types exposure time series, non-significant correlations (p-values>0.05) are represented as grey shaded cells.

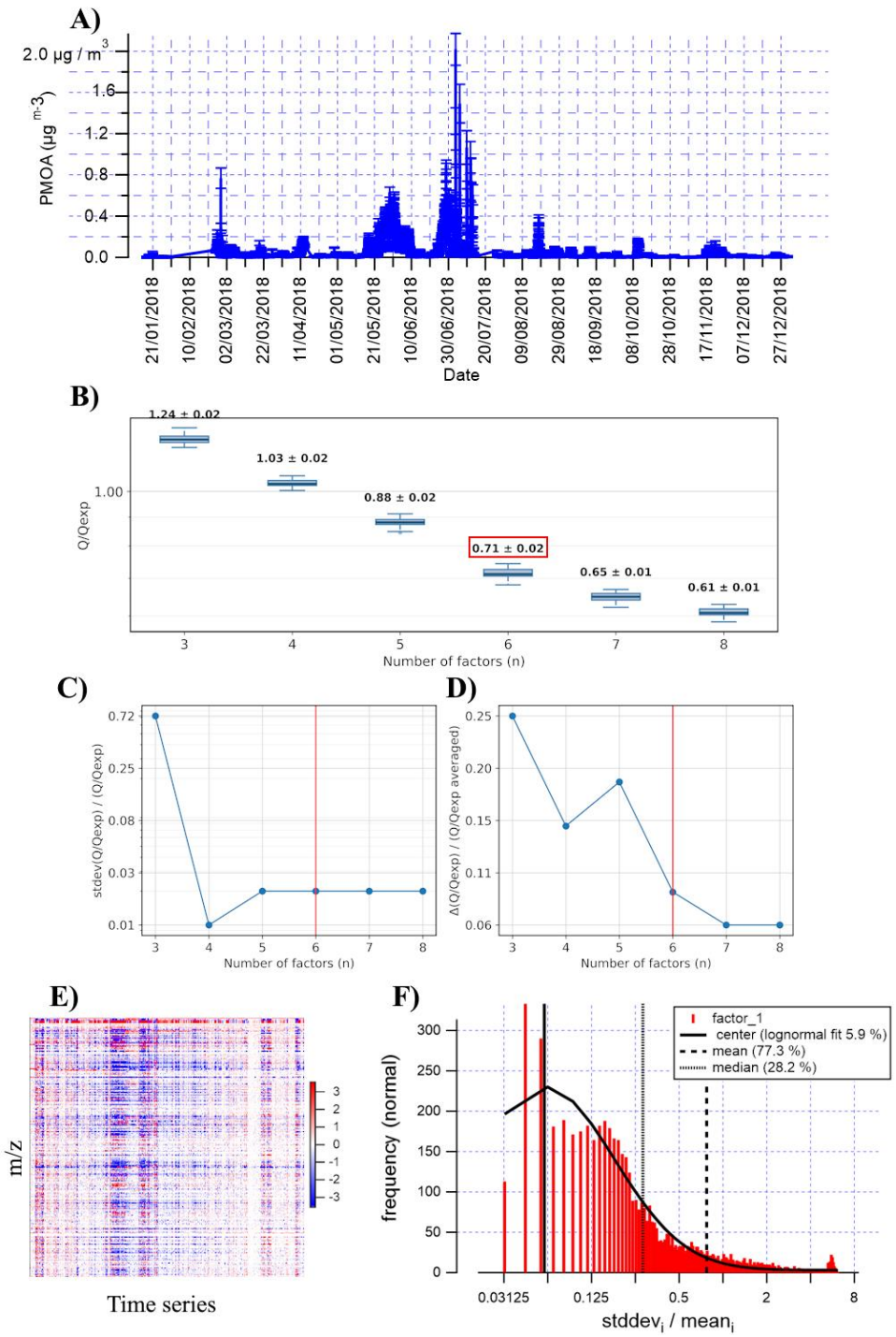

Figure S8. (A) PMOA time series (µg m⁻³) from the six-factor solution, expressed as the mean ± standard deviation across all bootstrap runs. (B) Distribution of Q/Qexp across bootstrap runs for factor solutions ranging from three to eight factors, with mean ± standard deviation indicated above each box. (C) Relative variability of Q/Qexp, expressed as the standard deviation divided by the mean across bootstrap runs, as a function of factor number. (D) Relative change in Q/Qexp between successive factor solutions, defined as Δ(Q/Qexp)/⟨Q/Qexp⟩ from n to n+1 factors. (E) Scaled residuals matrix (observed minus modelled) for the six-factor solution, (F) Distribution of relative uncertainty across bootstrap runs, with lognormal fit (solid line), mean (dashed line) and median (dotted line) indicated.

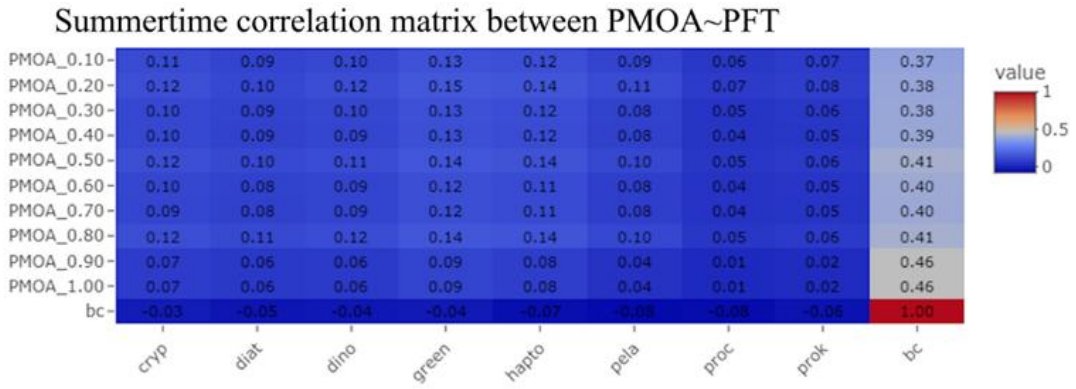

Figure S9. August 2018 - Pearson's correlations between primary marine organic aerosol (PMOA) constraining sensitivity analysis time series (a-values), black carbon (bc) and phytoplankton functional types HYSPLIT air masses exposure time series, non-significant correlations (p-values>0.05) are represented as grey shaded cells. Black carbon measurements are used as a counterfactual against truly pristine conditions.

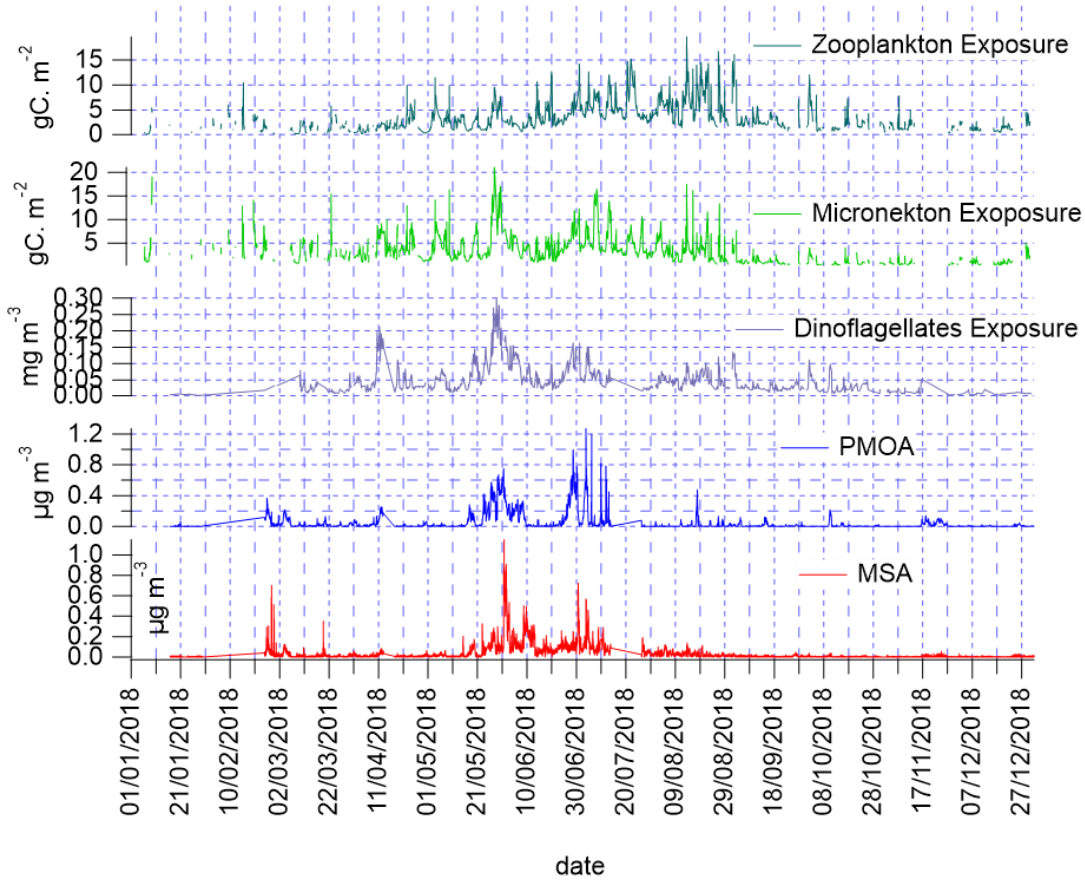

Figure S10. Time series of air-mass-integrated zooplankton and epipelagic micronekton exposure (gC m^{-2}), dinoflagellate exposure (mg m^{-3}), primary marine organic aerosol (PMOA, µg m^{-3}), and methane-sulphonic acid organic aerosol (MSA, µg m^{-3}) at Mace Head during 2018.

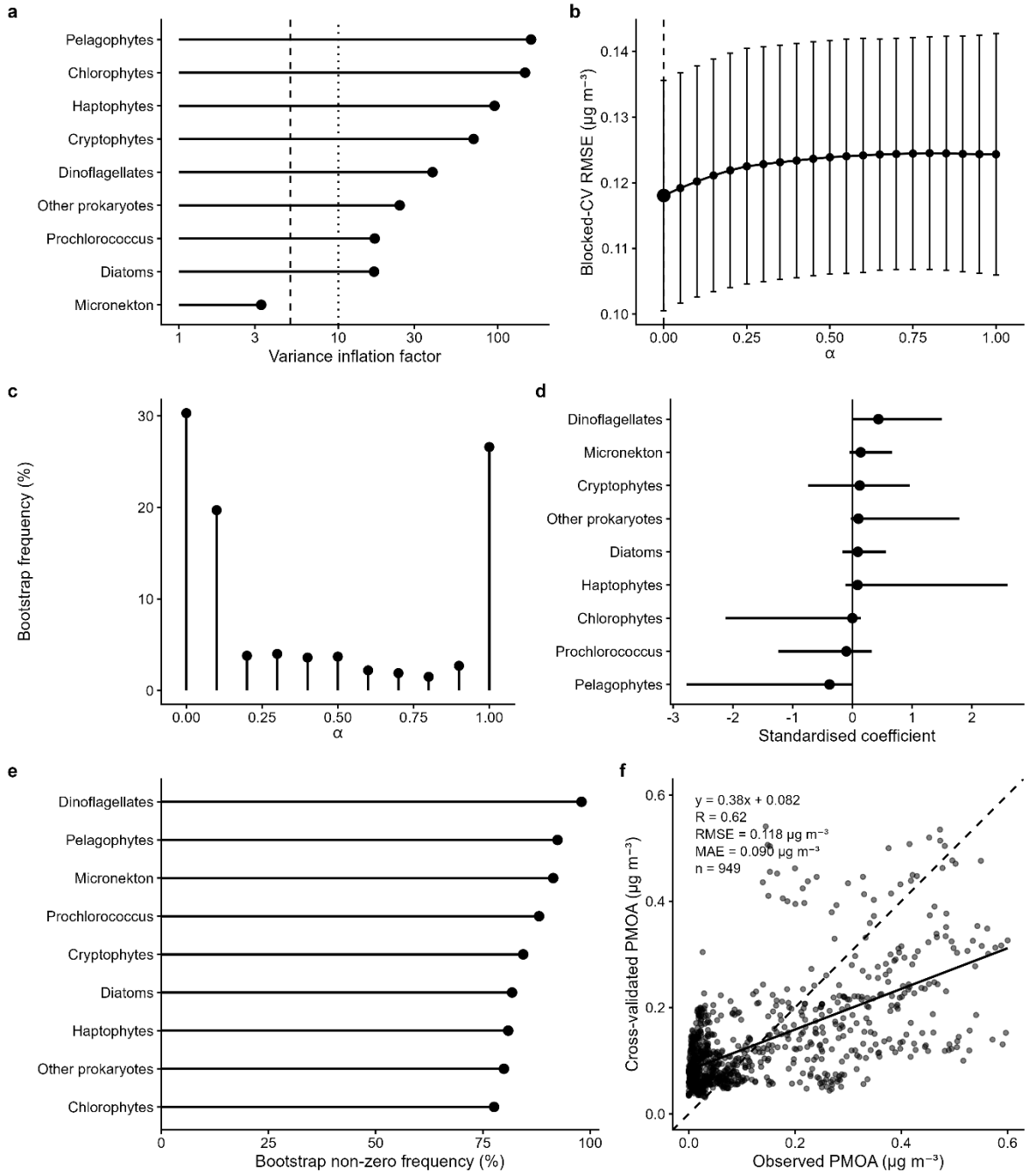

Figure S11. Collinearity and joint elastic-net attribution of PMOA to PFTs and micronekton (spring-summer climax, n = 949). a) Variance inflation factors (log scale; thresholds 5 and 10). b) Blocked-CV RMSE against α (± 1 SE; selected α = 0). c) Median standardised coefficients with 95 % bootstrap intervals (1000 moving-block replicates, 48 h blocks). d) α selected within replicates. e) Non-zero frequency across replicates. f) Observed against cross-validated PMOA (dashed 1:1 line, solid least-squares fit).

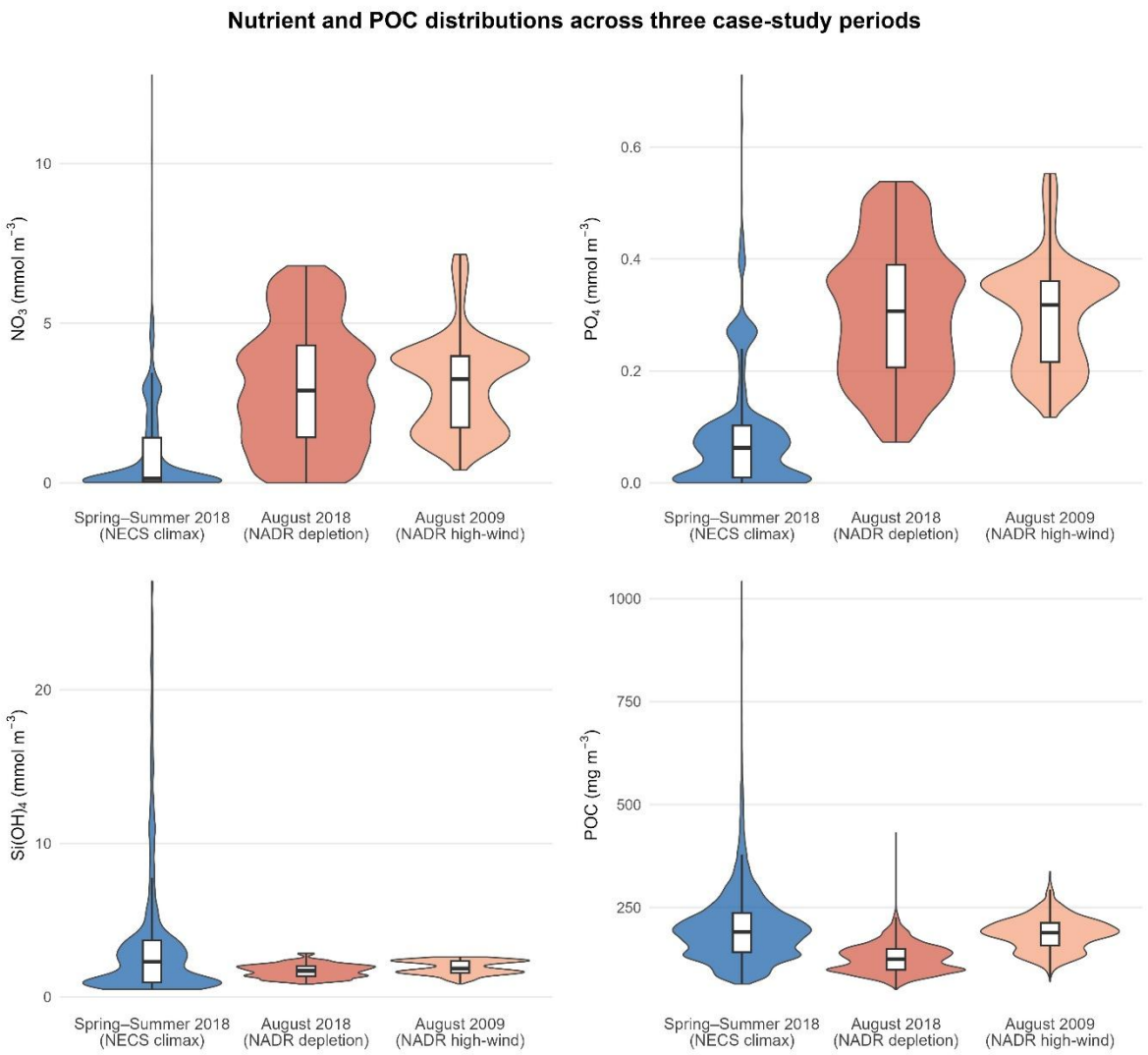

115

Figure S12. Distributions of NO_3, PO_4, $Si(OH)_4$, and particulate organic carbon (POC) across the three source-region periods. Boxes show medians and interquartile ranges.

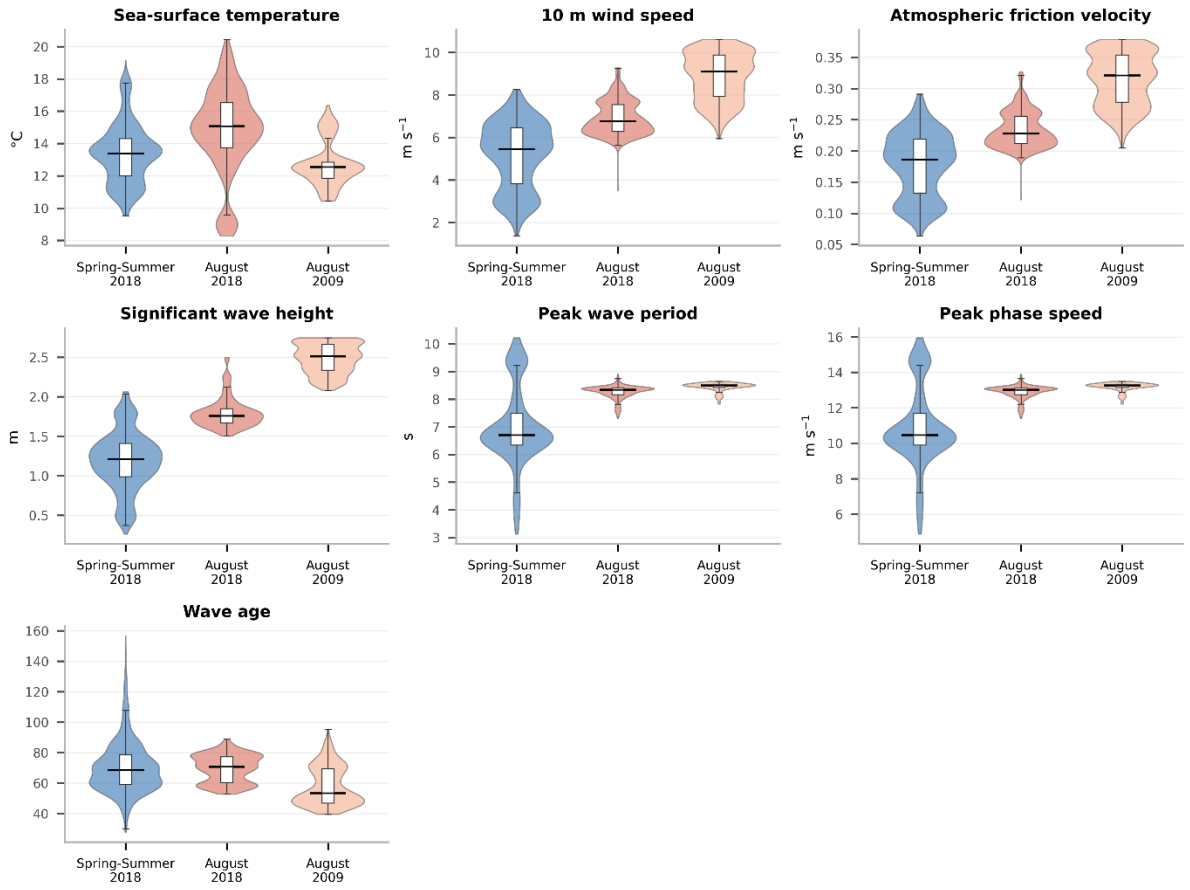

120 **Figure S13. Distributions of sea-surface temperature, 10 m wind speed, atmospheric friction velocity, significant wave height, peak wave period, peak phase speed, and wave age across the three source-region periods. Boxes show medians and interquartile ranges.**

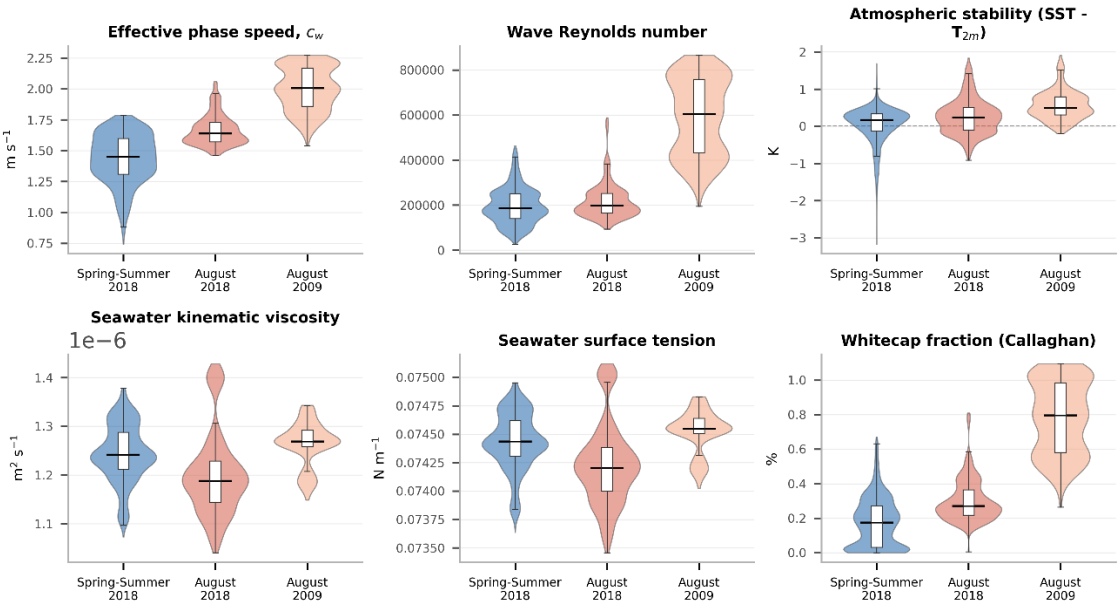

125 **Figure S14. Distributions of effective phase speed, wave Reynolds number, atmospheric stability, seawater kinematic viscosity, seawater surface tension, and whitecap fraction across the three source-region periods. Boxes show medians and interquartile ranges.**

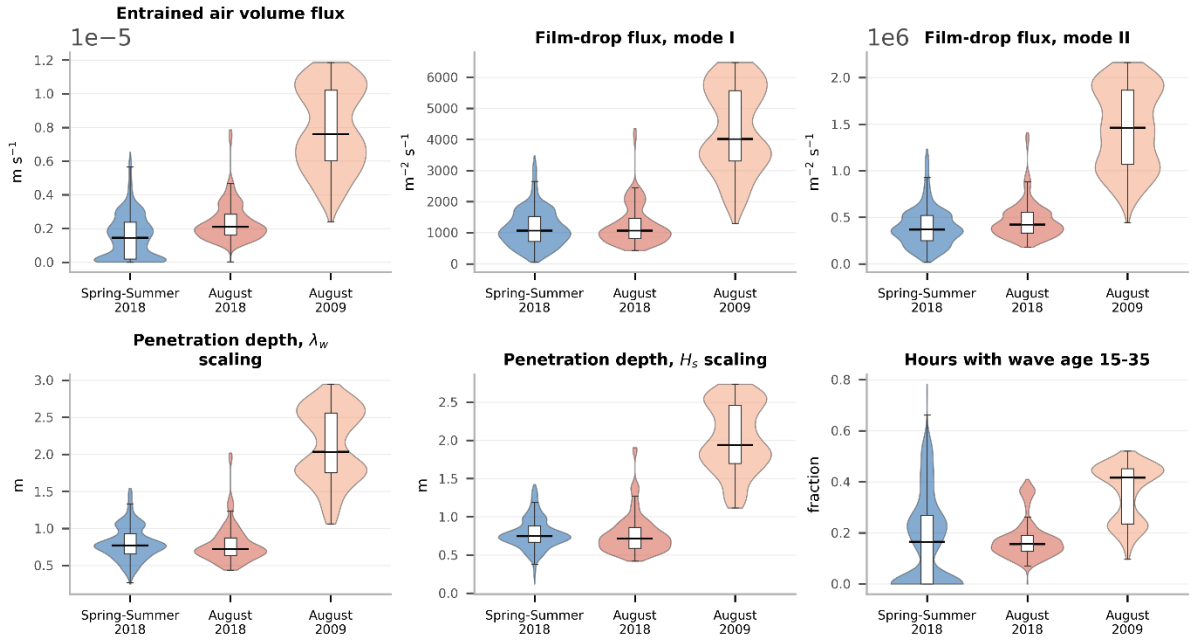

Figure S15. Distributions of entrained air volume flux, film-drop flux modes I and II, penetration depth under λw and *Hs* scaling, and fraction of hours with wave age 15-35 across the three source-region periods. Boxes show medians and interquartile ranges.

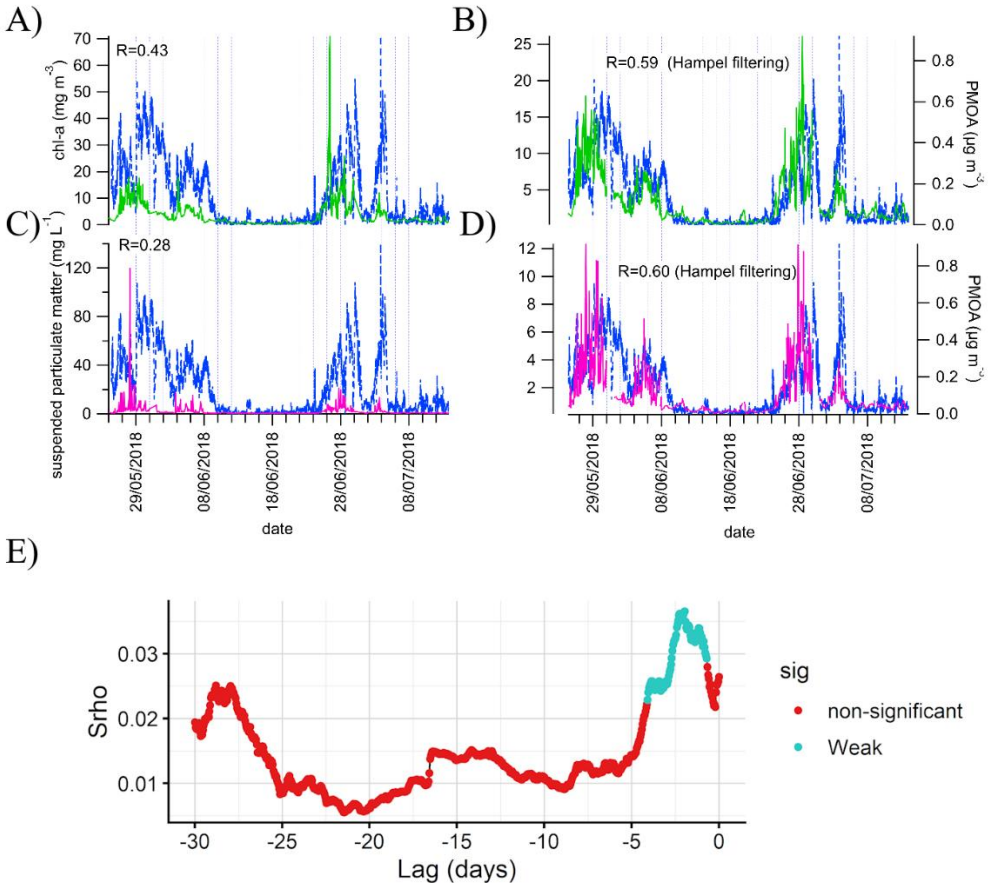

Figure S16. Time series of satellite-derived ocean colour variables compared with PMOA during the spring-summer climax period. Panels show (A) chlorophyll-*a* (chl-*a*), (B) Hampel-filtered chl-

***a*, (C) suspended particulate matter (SPM), and (D) Hampel-filtered SPM, F) Cross entropy between PMOA and Hampel filtered chl-*a*.**

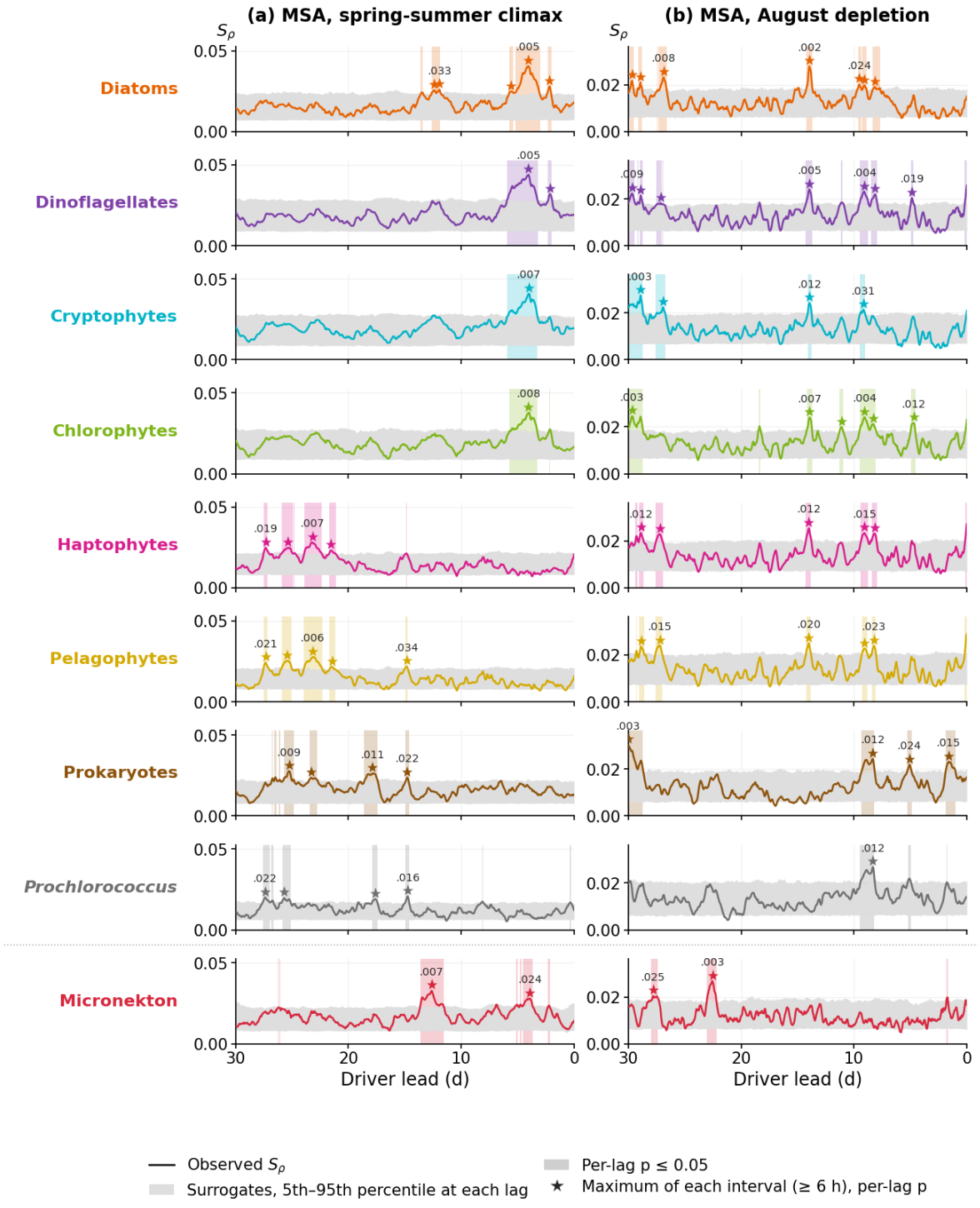

Figure S17. Lagged cross-entropy Sρ between MSA and air-mass exposure to the eight phytoplankton functional types (PFTs) and micronekton at Mace Head during (a) the spring-summer climax phase and (b) the August 2018 depletion phase. Coloured lines show the observed Sρ, and grey bands show the 5th-95th percentile of 1000 surrogates at each lag (multivariate IAAFT for the PFTs, univariate IAAFT for micronekton). Shading marks lags with a per-lag p value of 0.05 or less, where p is the share of surrogates with Sρ at least as large

as observed at that lag. Stars mark the maximum of each such interval lasting at least 6 h, and the number above a star is the per-lag p value at that maximum.

Text S1. Collinearity among biological predictors

To account for shared variability among PFT and micronekton, collinearity and joint attribution were subsequently evaluated during the spring-summer climax phase. VIFs ranged from 3.3 to 161.6 (**Table S3**), all PFT exceeded both conventional thresholds of 5 and 10, with micronekton (VIF = 3.3) being the only exception (**Figure S11a**, **Table S3**). The four most strongly inflated predictors, pelagophytes (VIF = 161.6), chlorophytes (148.2), haptophytes (95.4) and cryptophytes (70.5), are each reproduced from the remaining eight predictors with $R^2 > 0.985$, so their contributions are close to linearly dependent by construction. Dinoflagellates (39.0), other prokaryotes (24.3), *Prochlorococcus* (16.9) and diatoms (16.8) are less severely affected but still well above the threshold at which coefficient variance is considered inflated.

The cross-validation surface was almost flat in α, the blocked-CV RMSE varied only between 0.118 μg m^{-3} at α = 0 and 0.125 μg m^{-3} at α = 0.80, against a cross-validation standard error of approximately 0.018 μg m^{-3} (**Figure S11b**). Every value of α therefore lies within one standard error of the minimum, and the nominally optimal solution, α = 0 with λ = 0.093, is a pure ridge fit that retains all nine predictors.

Ranked by standardised coefficient, the ridge solution places dinoflagellates first (β = 0.18), followed by cryptophytes (0.15), diatoms (0.12), micronekton (0.12) and chlorophytes (0.10), with weaker contributions from *Prochlorococcus* (-0.089), pelagophytes (-0.055), other prokaryotes (0.042) and haptophytes (0.010) (**Table S4**). Elastic net regression therefore explains a fraction of PMOA variability (R = 0.62, RMSE = 0.118 μg m^{-3}, MAE = 0.090 μg m^{-3}) and can be expressed as follows using PFT in mg m^{-3} and micronekton in g C m^{-2}:

$$\text{PMOA}\ [\mu g\ m^{-3}] = 0.00391 + 0.507 \times \text{dinoflagellates} + 0.359 \times \text{cryptophytes} + 0.0454 \times \text{diatoms} + 0.00455 \times \text{micronekton} + 0.0835 \times \text{chlorophytes} - 1.68 \times \textit{Prochlorococcus} - 0.801 \times \text{pelagophytes} + 0.681 \times \text{other prokaryotes} + 0.0189 \times \text{haptophytes}$$

Table S1. Longhurst Regional variability in PFT composition

Region	Crypto-phytes (%)	Diatoms (%)	Dino-flagellates (%)	Chloro-phytes (%)	Hapto-phytes (%)	Pelago-phytes (%)	*Prochloro-coccus* (%)	Pro-karyotes (%)	Total (mg m^{-3})
NADR	6.9	24.4	5.0	31.1	23.7	3.1	3.3	2.5	0.48
ARCT	5.2	49.4	4.6	18.0	18.7	2.4	0.9	0.8	0.97
NECS	5.2	49.4	4.6	18.0	18.7	2.4	0.9	0.8	0.90
NWCS	8.7	53.9	5.2	20.7	6.7	1.0	2.0	1.8	0.83
SARC	5.6	45.0	5.4	22.8	17.4	2.0	0.8	1.0	0.77
BPLR	7.2	65.5	4.2	15.7	4.7	0.9	1.3	0.6	0.97
NASE	7.0	19.4	4.3	32.3	22.2	3.2	6.2	5.4	0.36

Region	Crypto-phytes (%)	Diatoms (%)	Dino-flagellates (%)	Chloro-phytes (%)	Hapto-phytes (%)	Pelago-phytes (%)	*Prochloro-coccus* (%)	Pro-karyotes (%)	Total (mg m^{-3})
GFST	6.3	22.9	4.6	30.8	18.4	2.8	7.6	6.7	0.31

Table S2. Pearson´s correlations between different phytoplankton groups and sea spray related measurements (PMOA in this study) across marine regions; data compiled from Moallemi *et al*. (2021a)[1], Jung *et al*. (2020)[2], Freney *et al*. (2020)[3], Trueblood *et al*. (2021)[4], Schwier *et al*. (2017)[5], Schwier *et al*. (2015)[6] and (Sellegri *et al*., 2021)[7]. NS: non-significant

PFT Measurements	This Study HR-ToF-AMS	Southern Ocean[1] SSF	Amundsen Sea[2] SSF	Med Sea[3] ToF-ACSM	Med Sea[4] INP	Med Sea[5] CCN	Med Sea[6] CCN	Med Sea[7] CCN
Cryptophytes	0.68			-0.22	0.48	0.58		
Diatoms	0.65		0.89			0.64		
Dinoflagellates	0.70	-0.4 0.4				0.64		
Chlorophytes	0.62	0.55 0.69						
Haptophytes	0.30	-0.4 0.4		-0.27–0.38	0.10–0.48			0.32
Pelagophytes	0.21	0.44						
Prochlorococcus	-0.02	-0.4 0.4					0.70	
Prokaryotes	0.32	-0.4 0.4		-0.41–0.28	NS			
Micronekton	0.55							

HR-ToF-AMS: High-Resolution Time-of-Flight Aerosol Mass Spectrometer; SSF: Sea Spray Fluorescence; ToF-ACSM: Time-of-Flight Aerosol Chemical Speciation Monitor; INP: Ice Nucleating Particles; CCN: Cloud Condensation Nuclei; NS: Not significant.

Table S3. Variance inflation factors for the eight phytoplankton functional types and micronekton over the spring-summer climax phase. Each predictor is regressed on the remaining eight; the coefficient of determination of that auxiliary regression, its tolerance (R^2) and the resulting VIF are reported.

Predictor	R^2 against other predictors	Tolerance	VIF
Pelagophytes	0.994	0.006	161.6
Chlorophytes	0.993	0.007	148.2
Haptophytes	0.990	0.010	95.4
Cryptophytes	0.986	0.014	70.5
Dinoflagellates	0.974	0.026	39.0
Other prokaryotes	0.959	0.041	24.3
Prochlorococcus	0.941	0.059	16.9
Diatoms	0.940	0.060	16.8
Micronekton	0.696	0.304	3.3

Table S4. Elastic-net coefficients and bootstrap stability for the joint attribution of PMOA to phytoplankton functional types and micronekton during the spring-summer climax phase. Model selected by five-fold blocked cross-validation ($\alpha = 0, \lambda = 0.093$). Standardised coefficients are expressed per standard deviation of predictor and of PMOA. Bootstrap statistics are from 1000 moving-block replicates with a 48 h block length and α and λ re-selected in each replicate. Sign stability is the fraction

of replicates sharing the modal sign. Blocked cross-validation performance: $R^2 = 0.38$, $R = 0.62$, RMSE = 0.118 μg m^{-3}, MAE = 0.090 μg m^{-3}.

Predictor	Standardised coefficient	Bootstrap median	Bootstrap 95 % interval	Non-zero frequency	Sign stability
Dinoflagellates	0.180	0.435	0.000 to 1.495	0.98	0.97
Cryptophytes	0.148	0.123	-0.738 to 0.957	0.84	0.64
Diatoms	0.121	0.091	-0.171 to 0.559	0.82	0.69
Micronekton	0.117	0.139	-0.047 to 0.663	0.91	0.86
Chlorophytes	0.097	0.000	-2.123 to 0.140	0.78	0.44
Prochlorococcus	-0.089	-0.101	-1.241 to 0.325	0.88	0.77
Pelagophytes	-0.055	-0.383	-2.778 to 0.000	0.92	0.92
Other prokaryotes	0.042	0.101	-0.029 to 1.788	0.80	0.75
Haptophytes	0.010	0.087	-0.118 to 2.596	0.81	0.61

Table S5. Median and interquartile range (IQR; P25-P75) of air-sea physical parameters, nutrients and particulate organic carbon (POC) across the spring-summer 2018 NECS climax, August 2018 NADR depletion, and August 2009 NADR high-wind source footprints.

Variable	Unit	Spring–summer 2018 (NECS climax)		August 2018 (NADR depletion)		August 2009 (NADR high-wind)	
		Median	IQR (P25–P75)	Median	IQR (P25–P75)	Median	IQR (P25–P75)
Sea-surface temperature (SST)	°C	1.34×10^{1}	1.20×10^{1}–1.43×10^{1}	1.51×10^{1}	1.37×10^{1}–1.65×10^{1}	1.25×10^{1}	1.19×10^{1}–1.28×10^{1}
10 m wind speed (U_{10})	m s^{-1}	5.45×10^{0}	3.82×10^{0}–6.45×10^{0}	6.76×10^{0}	6.29×10^{0}–7.55×10^{0}	9.10×10^{0}	7.94×10^{0}–9.88×10^{0}
Atmospheric friction velocity (u*)	m s^{-1}	1.86×10^{-1}	1.33×10^{-1}–2.19×10^{-1}	2.28×10^{-1}	2.12×10^{-1}–2.56×10^{-1}	3.21×10^{-1}	2.78×10^{-1}–3.54×10^{-1}
Air-sea temperature difference (SST − T_2m)	K	1.68×10^{-1}	-1.21×10^{-1}–3.34×10^{-1}	2.29×10^{-1}	-9.56×10^{-2}–5.13×10^{-1}	4.95×10^{-1}	3.12×10^{-1}–7.96×10^{-1}
Significant wave height (H_s)	m	1.21×10^{0}	9.91×10^{-1}–1.41×10^{0}	1.76×10^{0}	1.67×10^{0}–1.85×10^{0}	2.51×10^{0}	2.34×10^{0}–2.67×10^{0}
Peak wave period (T_p)	s	6.70×10^{0}	6.34×10^{0}–7.49×10^{0}	8.33×10^{0}	8.17×10^{0}–8.40×10^{0}	8.49×10^{0}	8.42×10^{0}–8.55×10^{0}
Peak phase speed (c_p)	m s^{-1}	1.05×10^{1}	9.89×10^{0}–1.17×10^{1}	1.30×10^{1}	1.27×10^{1}–1.31×10^{1}	1.33×10^{1}	1.31×10^{1}–1.33×10^{1}
Wave age (c_p/u*)	dimensionless	6.86×10^{1}	5.91×10^{1}–7.86×10^{1}	7.07×10^{1}	6.05×10^{1}–7.74×10^{1}	5.33×10^{1}	4.69×10^{1}–6.94×10^{1}
Effective wind-coupled phase speed (c_v)	m s^{-1}	1.45×10^{0}	1.31×10^{0}–1.60×10^{0}	1.64×10^{0}	1.57×10^{0}–1.73×10^{0}	2.01×10^{0}	1.86×10^{0}–2.17×10^{0}
Wave Reynolds number (ReHw)	dimensionless	1.86×10^{5}	1.41×10^{5}–2.51×10^{5}	1.98×10^{5}	1.65×10^{5}–2.53×10^{5}	6.04×10^{5}	4.32×10^{5}–7.58×10^{5}
Seawater kinematic viscosity (νw)	m^2 s^{-1}	1.24×10^{-6}	1.21×10^{-6}–1.29×10^{-6}	1.19×10^{-6}	1.14×10^{-6}–1.23×10^{-6}	1.27×10^{-6}	1.26×10^{-6}–1.29×10^{-6}
Seawater surface tension (γ)	N m^{-1}	7.44×10^{-2}	7.43×10^{-2}–7.46×10^{-2}	7.42×10^{-2}	7.40×10^{-2}–7.44×10^{-2}	7.45×10^{-2}	7.45×10^{-2}–7.46×10^{-2}
Whitecap fraction	%	1.75×10^{-1}	3.11×10^{-2}–2.71×10^{-1}	2.70×10^{-1}	2.18×10^{-1}–3.65×10^{-1}	7.95×10^{-1}	5.80×10^{-1}–9.84×10^{-1}
Entrained air volume flux	m s^{-1}	1.45×10^{-6}	1.85×10^{-7}–2.38×10^{-6}	2.10×10^{-6}	1.61×10^{-6}–2.84×10^{-6}	7.60×10^{-6}	6.03×10^{-6}–1.02×10^{-5}
Total film-drop number flux	m^{-2} s^{-1}	3.69×10^{5}	2.49×10^{5}–5.22×10^{5}	4.20×10^{5}	3.33×10^{5}–5.54×10^{5}	1.46×10^{6}	1.07×10^{6}–1.87×10^{6}
Bubble-plume penetration depth (λw scaling)	m	7.73×10^{-1}	6.59×10^{-1}–9.30×10^{-1}	7.23×10^{-1}	6.33×10^{-1}–8.74×10^{-1}	2.03×10^{0}	1.75×10^{0}–2.56×10^{0}
Bubble-plume penetration depth (H_s scaling)	m	7.46×10^{-1}	6.68×10^{-1}–8.78×10^{-1}	7.15×10^{-1}	5.89×10^{-1}–8.62×10^{-1}	1.94×10^{0}	1.70×10^{0}–2.46×10^{0}
Nitrate (NO_3^-)	mmol m^{-3}	1.40×10^{-1}	3.64×10^{-2}–1.42×10^{0}	2.89×10^{0}	1.43×10^{0}–4.31×10^{0}	3.25×10^{0}	1.74×10^{0}–3.97×10^{0}
Phosphate (PO_4^{3-})	mmol m^{-3}	6.27×10^{-2}	9.74×10^{-3}–1.03×10^{-1}	3.07×10^{-1}	2.06×10^{-1}–3.90×10^{-1}	3.18×10^{-1}	2.16×10^{-1}–3.61×10^{-1}
Silicate (Si)	mmol m^{-3}	2.29×10^{0}	9.37×10^{-1}–3.68×10^{0}	1.70×10^{0}	1.35×10^{0}–2.00×10^{0}	1.85×10^{0}	1.57×10^{0}–2.34×10^{0}
Particulate organic carbon (POC)	mg m^{-3}	1.91×10^{2}	1.42×10^{2}–2.36×10^{2}	1.24×10^{2}	9.85×10^{1}–1.49×10^{2}	1.89×10^{2}	1.58×10^{2}–2.13×10^{2}

References

Freney, E., Sellegri, K., Nicosia, A., Trueblood, J.T., Rinaldi, M., Williams, L.R., Prévôt, A.S.H., Thyssen, M., Grégori, G., Haëntjens, N., Dinasquet, J., Obernosterer, I., Van-Wambeke, F., Engel, A., Zäncker, B., Desboeufs, K., Asmi, E., Timmonen, H., Guieu, C., 2020. Mediterranean nascent sea spray organic aerosol and relationships with seawater biogeochemistry (preprint). Aerosols/Field Measurements/Troposphere/Chemistry (chemical composition and reactions). https://doi.org/10.5194/acp-2020-406

Jung, J., Hong, S.-B., Chen, M., Hur, J., Jiao, L., Lee, Y., Park, K., Hahm, D., Choi, J.-O., Yang, E.J., Park, J., Kim, T.-W., Lee, S., 2020. Characteristics of methanesulfonic acid, non-sea-salt sulfate and organic carbon aerosols over the Amundsen Sea, Antarctica. Atmos. Chem. Phys. 20, 5405–5424. https://doi.org/10.5194/acp-20-5405-2020

Mansour, K., Decesari, S., Ceburnis, D., Ovadnevaite, J., Russell, L.M., Paglione, M., Poulain, L., Huang, S., O'Dowd, C., Rinaldi, M., 2024. IPB-MSA&SO_4 : a daily 0.25° resolution dataset of in situ-produced biogenic methanesulfonic acid and sulfate over the North Atlantic during 1998–2022 based on machine learning. Earth Syst. Sci. Data 16, 2717–2740. https://doi.org/10.5194/essd-16-2717-2024

Moallemi, A., Landwehr, S., Robinson, C., Simó, R., Zamanillo, M., Chen, G., Baccarini, A., Schnaiter, M., Henning, S., Modini, R.L., Gysel-Beer, M., Schmale, J., 2021. Sources, Occurrence and Characteristics of Fluorescent Biological Aerosol Particles Measured Over the Pristine Southern Ocean. JGR Atmospheres 126, e2021JD034811. https://doi.org/10.1029/2021JD034811

Ovadnevaite, J., O'Dowd, C., Dall'Osto, M., Ceburnis, D., Worsnop, D.R., Berresheim, H., 2011. Detecting high contributions of primary organic matter to marine aerosol: A case study. Geophysical Research Letters 38. https://doi.org/10.1029/2010GL046083

Schwier, A.N., Rose, C., Asmi, E., Ebling, A.M., Landing, W.M., Marro, S., Pedrotti, M.-L., Sallon, A., Iuculano, F., Agusti, S., Tsiola, A., Pitta, P., Louis, J., Guieu, C., Gazeau, F., Sellegri, K., 2015. Primary marine aerosol emissions from the Mediterranean Sea during pre-bloom and oligotrophic conditions: correlations to seawater chlorophyll *a* from a mesocosm study. Atmos. Chem. Phys. 15, 7961–7976. https://doi.org/10.5194/acp-15-7961-2015

Schwier, A.N., Sellegri, K., Mas, S., Charrière, B., Pey, J., Rose, C., Temime-Roussel, B., Jaffrezo, J.-L., Parin, D., Picard, D., Ribeiro, M., Roberts, G., Sempéré, R., Marchand, N., D'Anna, B., 2017. Primary marine aerosol physical flux and chemical composition during a nutrient enrichment experiment in mesocosms in the Mediterranean Sea. Atmos. Chem. Phys. 17, 14645–14660. https://doi.org/10.5194/acp-17-14645-2017

Sellegri, K., Nicosia, A., Freney, E., Uitz, J., Thyssen, M., Grégori, G., Engel, A., Zäncker, B., Haëntjens, N., Mas, S., Picard, D., Saint-Macary, A., Peltola, M., Rose, C., Trueblood, J., Lefevre, D., D'Anna, B., Desboeufs, K., Meskhidze, N., Guieu, C., Law, C.S., 2021. Surface ocean microbiota determine cloud precursors. Sci Rep 11, 281. https://doi.org/10.1038/s41598-020-78097-5

Trueblood, J.V., Nicosia, A., Engel, A., Zäncker, B., Rinaldi, M., Freney, E., Thyssen, M., Obernosterer, I., Dinasquet, J., Belosi, F., Tovar-Sánchez, A., Rodriguez-Romero, A., Santachiara, G., Guieu, C., Sellegri, K., 2021. A two-component parameterization of marine ice-nucleating particles based on seawater biology and sea spray aerosol measurements in the Mediterranean Sea. Atmos. Chem. Phys. 21, 4659–4676. https://doi.org/10.5194/acp-21-4659-2021

Zhang, Y., Shen, F., Li, R., Li, M., Li, Z., Chen, S., Sun, X., 2024. AIGD-PFT: the first AI-driven global daily gap-free 4 km phytoplankton functional type data product from 1998 to 2023. Earth Syst. Sci. Data 16, 4793–4816. https://doi.org/10.5194/essd-16-4793-2024